2008-07-10

Early Dynamics of Ultracold Neutral Plasmas

Adam W. Denning
Brigham Young University - Provo

BYU ScholarsArchive Citation

Denning, Adam W., "Early Dynamics of Ultracold Neutral Plasmas" (2008). *All Theses and Dissertations*. 1469.
https://scholarsarchive.byu.edu/etd/1469

EARLY DYNAMICS OF ULTRACOLD NEUTRAL PLASMAS

by

Adam W. Denning

A thesis submitted to the faculty of

Brigham Young University

in partial fulfillment of the requirements for the degree of

Master of Science

Department of Physics and Astronomy

Brigham Young University

August 2008

BRIGHAM YOUNG UNIVERSITY

GRADUATE COMMITTEE APPROVAL

of a thesis submitted by

Adam W. Denning

This thesis has been read by each member of the following graduate committee and by majority vote has been found to be satisfactory.

Date Scott D. Bergeson, Chair

Date Michael J. Ware

Date Dallin S.Durfee

BRIGHAM YOUNG UNIVERSITY

As chair of the candidate's graduate committee, I have read the thesis of Adam W. Denning in its final form and have found that (1) its format, citations, and bibliographical style are consistent and acceptable and fulfill university and department style requirements; (2) its illustrative materials including figures, tables, and charts are in place; and (3) the final manuscript is satisfactory to the graduate committee and is ready for submission to the university library.

Date

Scott D. Bergeson
Chair, Graduate Committee

Accepted for the Department

J. Ward Moody, Graduate Coordinator
Department of Physics and Astronomy

Accepted for the College

Thomas W. Sederberg, Associate Dean
College of Mathematics and Physical Sciences

ABSTRACT

EARLY DYNAMICS OF ULTRACOLD NEUTRAL PLASMAS

Adam W. Denning

Department of Physics and Astronomy

Master of Science

We report new studies on the early-time dynamics of ultracold neutral plasmas. We use fluorescence spectroscopy to probe plasma dynamics on the nanosecond time scale. We determine the rms ion velocity during the initial plasma period. The initial ion acceleration is found as the time derivative of the ion velocity. We compare to a theoretical model. The experimental results agree with the model at low plasma densities. However, the ion acceleration is a factor of ten lower than the model at higher densities. The cause of this discrepancy is currently unknown.

ACKNOWLEDGMENTS

I am not a typical physics student. I did not study hard in high school in preparation for college or even take college placement exams. I was not interested in mathematics or much anything else academically. Though, as a child I did often wonder about nature. I was continually a "D-" student until my senior year in high school in which I was forced to do well in order to graduate. Upon graduation I had never taken a physics course and to be quite honest I was not sure what physics was.

I would first like to thank my wife. She has sacrificed constantly to make this possible and always provided emotional, financial, and scholarly support. I want to thank her for the lovely baby she has given me; she and Sophia are the light of my life and the heart of my inspiration. I happily give them all that I am.

I would like to thank Paul Mills for his outstanding teaching. He made learning physics invigorating and fun. Thanks to Alvin K. Benson for his patience, understanding, his listening ear, and just being on my wavelength. Finally I would like to thank my advisor Scott Bergeson for reaching out to me and having faith in my abilities. I would like to thank him for what seems like infinite patience and for always pushing me. I would like to thank him for his example he sets at home, school, and in the atomic physics community. It has been an honor and a privilege to be his student.

I would also like to express my appreciation of learning in a conducive

environment such as BYU. I am grateful to the department of physics and astronomy for giving me a chance to earn a higher education. I would also like to thank faculty members such as Dallin Durfee, Michael Ware, Kent Gee, Scott Daniel, Ross Spencer, and David Allred who have graciously given help to me when needed. I would also like to thank Nan Ah You and Diann Sorensen for putting up with my unexpected demands and tardiness.

Last, but not least, I want to express my appreciation to the National Science Foundation. Without its financial support (Grant number PHY-0601699), my research project could not have been done.

Contents

List of Figures

Chapter 1

Introduction

More than 99% of the visible Universe is plasma. A plasma is an ionized gas that exhibits collective behavior. Plasmas form localized pockets of charge that give rise to electric fields. Charged particles accelerate and give rise to magnetic fields. These electric and magnetic fields are responsible for the collective behavior of particles in plasmas.

Plasmas are classified by temperature, T_e, and density, n, where density is the number of ions or electrons per unit volume. The Debye length, the length over which electric fields are screened, is dependent on temperature and density, $\lambda_D = \sqrt{\epsilon_0 k_B T_e / n e^2}$. Most plasmas are hot ($10^4 - 10^7$ K) and range widely in density ($10^3 - 10^{33}$ charged particles per m^3). The temperatures are high enough that collisions between particles are energetic enough to ionize the atoms. For example the solar core has an electron temperature of 10^7 K with density around 10^{32} per m^3. Some regions of interstellar space are a low density plasma of 10^5 per m^3 and a temperature of 8000 K. The temperature of lightning is around $30,000$ K with relatively high density approximately 10^{21} per m^3.

Plasmas may also be cold. Cold plasma temperatures are in the room temperature to sub Kelvin temperature range. These plasmas are not in thermodynamic equilibrium. Initially cold plasmas may be strongly coupled, meaning the ratio of the local electric potential energy to the kinetic energy is larger than one. This ratio is characterized by the strong coupling parameter, $\Gamma \equiv e^2 n^{1/3}/4\pi\epsilon_0 k_B T$ [1]. Strongly coupled systems exhibit many interesting effects such as Coulomb crystallization, glassy behavior, approach to condensed matter system, breakdown of the binary collision approximation, and the breakdown of the fluid approximation.

Some examples of ultracold strongly coupled plasmas are dusty plasmas, non-neutral plasmas, and ultracold neutral plasmas. Dusty plasmas contain dust particles that have accumulated charge which drive the collective effects of the plasma. A unique property of dusty plasmas is the low charge to mass ratio of the particles. Non-neutral plasmas are formed by capturing ions in a trap. These ions are then laser cooled to mili-Kelvin temperatures. These plasmas are not electrically screened by electrons. Therefore, when the cooling lasers are turned off these plasmas expand rapidly as a coulomb explosion.

The initial temperature of ultracold neutral plasmas (UNPs) in our lab is around 1 mK [1]. UNPs are interesting because they are low temperature, strongly coupled, and electrically neutral. The initial random nature of UNPs creates a non-equilibrated system in which ions are quickly heated. This phase is called disorder induced heating (DIH). Theoretical work describing DIH has been proposed, however the theory has only been verified over a small range of densities and electron temperatures. The purpose of this study is to experimentally measure the ion acceleration during DIH over a broader range of densities and electron temperatures.

1.1 Characteristics of Ultracold Neutral Plasmas

Most UNPs are created by photo ionizing atoms in a magneto-optical trap. Consequently their density profiles are approximately Gaussian. A plasma density at time t is approximately

$$n(r,t) = n_0 \exp[-r^2/2\sigma^2(t)]\,[\sigma_0/\sigma(t)]^3\,, \tag{1.1}$$

where n_0 is the peak density, σ_0 is the initial plasma size, $\sigma(t) = \sqrt{\sigma_0^2 + v_{exp}^2 t^2}$ is the Gaussian radius of the plasma, and $v_{exp} = \sqrt{kT_e/m_i}$ is the expansion velocity. Peak densities of UNPs can be varied from 10^{13} - 10^{16} ions per m^3. Initial ion temperatures of plasmas in the ultracold regime are on the order of 1 mK, and the corresponding initial electron temperatures can be as low as 1K.

The term that plasma physicists use to describe the net charge of a plasma is neutrality, the ratio of free electrons to ions, $N \equiv n_e/n_o$. The neutrality of the plasma for a given electron temperature increases with the ion density [2]. It is approximately zero until the Debye length is less than or equal to the plasma size σ_0. Figure 1.1 shows the charge neutrality, $n_e/n_0 = 1 - (\lambda_D/\sigma_0)^2$, for three electron temperatures over a range of densities. The majority of data in our experiment exceeds 10^{14} per m^3. Therefore the neutrality of our plasmas is 94% or greater.

1.2 Time Evolution of Ultracold Neutral Plasmas

When the plasma is formed, the ions are randomly distributed in space. The initial ion kinetic energy is $E_i/k_B = 1$ mK. However, the nearest-neighbor ion-ion electrical potential energy can be 1000 times greater, in the 1K range. The ions move to minimize their potential energy. They oscillate in a complicated local potential formed by free electrons and neighboring plasma ions. This initial equilibration of the ions is

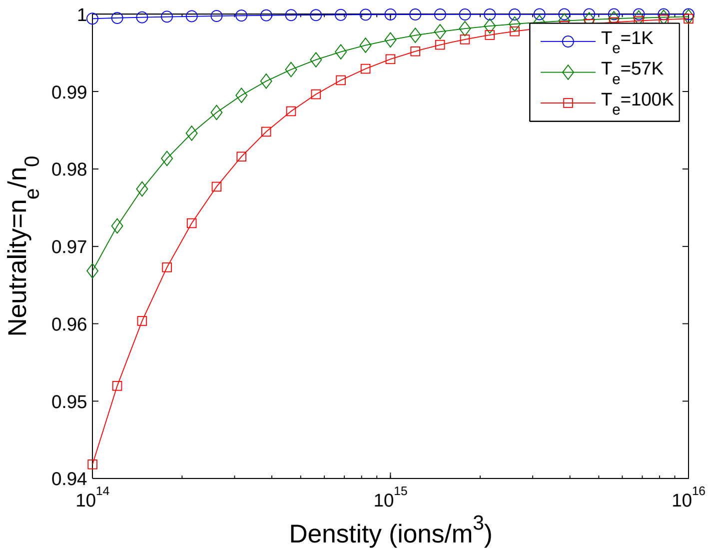

Figure 1.1 The charge neutrality of ultracold neutral plasmas versus density for three electron temperatures.

called disorder-induced heating (DIH). It occurs on the time scale of the inverse ion plasma frequency. In our experiments, this is near 100 ns. Obviously, the shape of local potential affects the rate at which DIH occurs.

The UNPs expand radially in a self-similar (Gaussian) manner, as shown in Eq. 1.1. The expansion is driven by electron pressure (the force exerted by the electrons on the ions as they as they try to leave the plasma) [3] and is characterized by an expansion velocity, $v_{\text{exp}} = \sqrt{k_B T_e/m_i}$, where T_e is the initial electron temperature and m_i is the ion mass. The time scale for expansion is determined by v_{exp} and the initial plasma size. When $\sigma_0 \sim 350$ μm, and $v_{exp} = 100$ m/s, then $t_{exp} = \sigma_0/v_{exp} = 3.5$ μs.

1.3 Experimental Techniques

A radio frequency technique (rf) [1] was first used to measure densities of UNPs as a function of time. The rf method can be used to measure densities over four orders of magnitude, from $10^{11} - 10^{15}$ per m^3. In this method an rf signal of known frequency is continuously directed into the plasma. As the plasma expands the average density decreases. At some time during the expansion the plasma frequency is in resonance with the rf signal

$$f_{\mathrm{rf}} = \omega_p/2\pi = (1/2\pi)\sqrt{e^2 n/\epsilon_0 m_i}. \tag{1.2}$$

When this occurs the plasma will oscillate and eject electrons. These charged particles are then accelerated via an applied DC electric field towards a detector. The number of incident electrons is measured as a function of time. The average density for a particular frequency is determined at the time of the peak signal using Eq. 1.2. The rf signal is absorbed over a broad spatial range the plasma. Therefore, the rf technique can not provide spatial information about the density profile [4].

A more recent technique for measuring characteristics of UNPs is absorption imaging [5]. This technique can spatially image the density profile as well as measure ion dynamics. During absorption imaging the plasma is illuminated by a collimated laser beam that has a diameter larger than the plasma diameter. The laser is tuned to the resonance of the first excited state of the ions. The laser intensity is absorbed according to Beer's Law, $I = I_0 \exp[OD]$, where OD is the optical depth. Laser intensity images are measured using a CCD camera with and without the plasma. The ratio of these images is processed to determine the ion density and temperature;

$$\begin{aligned} OD(x,y,z) &= ln[I_{\mathrm{back}}/I_{\mathrm{plasma}}] \\ &= \alpha(\nu)\int dz\; n_i(x,y,z) \\ &= \sqrt{2\pi}\alpha(\nu) n_o \sigma_z \exp\left(-x^2/2\sigma_x^2 - y^2/2\sigma_y^2\right) \end{aligned} \tag{1.3}$$

where n_o is the peak ion density, $\alpha(\nu)$ is the absorption cross section, and σ_z is the

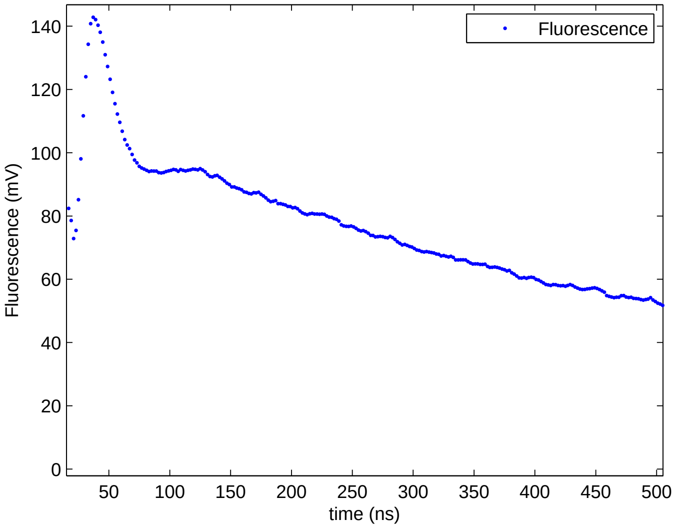

Figure 1.2 A typical UNP fluorescence signal over the first 500 ns. The data was recorded using a PMT and averaged using a digital oscilloscope.

$e^{-1/2}$ radius of the plasma in the z direction.

Finding how the temperature/velocity of the ions evolve in time requires knowledge of the spectral line width. The absorption spectra can be determined by recording the peak optical depth as a function of the detuning of the imaging beam. This spectra is fit to a Voigt profile in which the Lorenztian width is equal to the natural line width and the Gaussian width is used as a fit parameter. The Gaussian width consists of the random thermal motion of the ions as well as the directed motion of the expansion. Because the ion expansion is self-similar, the Gaussian spatial profile maps directly into a Gaussian velocity profile. The expansion masks the thermal motion at times longer than the average plasma period $1/\langle\omega_p\rangle$.

Time resolution of this method is limited to time delays associated with CCDs. There is a 10 ns time delay involved with initiating the exposure of the CCD. Typical minimal exposure times are on the order of tens of nanoseconds.

In our laboratory, we have developed the method of fluorescence spectroscopy [6].

This method is ideal for investigating plasma dynamics on the nanosecond time scale. In fluorescence spectroscopy a laser beam that is small in diameter compared to the plasma is directed directed through the center of the plasma. This laser beam is tuned to the first resonance transition of the ions so it is absorbed then scattered by the ions in all directions. Some of this fluorescence is collected using a lens and detected using a photo-multiplier tube (PMT). The key idea of fluorescence spectroscopy is that as the ions accelerate, the spectral linewidth increases due to Doppler broadening. Thus, a rise in velocity (or temperature) will correspond to a drop in the fluorescence signal. When determining ion dynamics, fluorescence spectroscopy has several advantages over absorption spectroscopy:

- Every data point of the fluorescence curve is translated to a velocity whereas absorption imaging requires multiple data points,
- Faster and simpler data processing,
- Improved signal to noise ratio,
- Time resolution on the 1 ns timescale.

Figure 1.2 shows an averaged fluorescence signal of a UNP during the first 500 ns after plasma creation. The rapid rise in the signal occurs as the ions begin to scatter photons from the probe laser beam (see Sec. 3.2). As the plasma heats during the DIH stage ($0 - 60$ ns) the fluorescence rapidly falls. Beyond 100 ns, the plasma ions begin a hydrodynamic expansion, the fluorescence continues to fall as the plasma dissipates.

Chapter 2

Early Time Dynamics

The majority of work done with UNPs has been directed toward ion equilibrium and expansion. Much is now known about the physics of UNPs during longer timescales. However, there is still much to learn about UNPs during early time scales. The early time scale is considered to be the time of initial plasma creation to end of the first plasma period. This is also known as the DIH phase. There are no detailed experimental studies focusing on ion dynamics in the 0-500 ns time scales.

A sophisticated and detailed simulation of the DIH process was recently published [7]. The molecular dynamics (MD) simulation used $10,000$ particles to track the acceleration of ions from the plasma micro-field during the DIH phase. This work revealed that, to the first order, DIH is dominated by nearest neighbor interactions and that many-body plasma effects do not begin until after the first inverse plasma frequency. One limitation of this study is that the electrons are treated as a fluid. This may gloss over electron/ion interaction at early times, especially when recombination is important.

Experimentally we are interested in measuring the ion acceleration during the DIH heating phase. Our goal is to determine how DIH acceleration is affected by the electron temperature and initial ion density.

2.1 Molecular Dynamic Model

The recent MD simulation provides us with a helpful model which will be introduced here. Murillo [7] observed that the ion temperature as a function of time should evolve as,

$$T_i(t) = T_i(0) + (t/\tau_2)^2 + (t/\tau_4)^4 + ..., \tag{2.1}$$

where τ_2 and τ_4 are expansion parameters from theory. The expressions for each are described in detail in by Murrilo's work [7]. The temperature has the units of $e^2/4\pi\epsilon_0 a_{ws} k_B$, where a_{ws} is the Wigner-Seitz radius or average distance between particles and k_B is the Boltzman constant. Time has units of inverse plasma frequency ω_p^{-1} (see Eq. 1.2), the average frequency ions oscillate in their potential well. We will drop the constant term as it is small compared to the quadratic term for times greater than 1 ns. Furthermore the quartic term may be neglected for early times (such as the first plasma period). After conversion into more familiar MKS units, Eq. 2.1 can be written as

$$\frac{3}{2}k_b T_i(t) = \frac{3}{2}\frac{e^2}{4\pi\epsilon_0 a_{ws}}\left(\frac{t\omega_p}{\tau_2}\right)^2 = \frac{1}{2}m_i v_i^2. \tag{2.2}$$

Solving for the ion velocity gives

$$\begin{aligned} v_i^2 &= \frac{1}{a_{ws}}\frac{3}{4\pi n}\frac{ne^2}{m_i\epsilon_0}\left(\frac{t\omega_p}{\tau_2}\right)^2 \\ &= a_{ws}^2(\omega_p^2)^2\left(\frac{t}{\tau_2}\right)^2, \end{aligned} \tag{2.3}$$

using the relations $a_{ws}^3 = 3/4\pi n$ and $w_p^2 = ne^2/m_i\epsilon_0$.

Assuming constant density, the acceleration is a time derivative of the velocity,

$$a = \frac{a_{ws}\omega_p^2}{\tau_2}, \tag{2.4}$$

where $1/\tau_2 = \sqrt{\langle F^2 \rangle}/3$ and $\langle F^2 \rangle$ represents the initial forces on the ions from the newly created potential landscape in dimensionless units.

Electron screening is often parameterized using a dimensionless ratio of the Wigner-Seitz radius to the Debye length, $\kappa \equiv a_{ws}/\lambda_D$. Results from the MD simulation [7] reveal $\langle F^2 \rangle$ to be a quasi-universal slowly varying function of κ,

$$\left\langle F^2 \right\rangle = 33 - 4\kappa + 0.1\kappa^2. \tag{2.5}$$

Equation 2.4 becomes

$$\begin{aligned} a &= a_{ws}\omega_p^2 \frac{\sqrt{33 - 4\kappa + 0.1\kappa^2}}{3} \\ &= a_{ws}\omega_p^2 \mathrm{G}_1(\kappa), \end{aligned} \tag{2.6}$$

where $\mathrm{G}_1(\kappa)$ is a slowly varying function of κ.

2.2 Nearest Neighbor Model

Since DIH is thought to be dominated by nearest neighbors we thought it useful to derive a model with the concepts of basic physics. Though this model will not be used in analysis, it solidifies results of the MD model and provides a conceptual explanation of DIH acceleration. Like the MD simulation [7] it is based on the Yukawa potential which is useful to model how electrons screen ions during the initial plasma evolution. In one dimension, the Yukawa potential is,

$$u = \frac{e^2}{4\pi\epsilon_0}\frac{\exp(-r/\lambda_D)}{r} \tag{2.7}$$

where r is the distance from the ion and λ_D is the screening length. The acceleration of a test particle located at distance a_{ws} due to this potential is easily obtained by taking the negative spatial derivative and dividing by the mass of the ion, m_i.

$$\begin{aligned} a &= -\frac{1}{m_i}\frac{du}{dr} = \frac{e^2}{4\pi\epsilon_0 m_i}\frac{du}{dr}\left[\frac{\exp(-r/\lambda_D)}{r}\right]|_{r=a_{ws}} \\ &= \frac{e^2}{4\pi\epsilon_0 m_i}\left(\frac{1}{\lambda_D r}+\frac{1}{r^2}\right)\exp(-r/\lambda_D)\,|_{r=a_{ws}} \end{aligned} \tag{2.8}$$

By pulling a term $1/r^2$ from the bracket, evaluating r at a_{ws}, then multiplying by $1 = a_{ws}/a_{ws}$, Eq. 2.8 becomes,

$$\begin{aligned} a &= \frac{a_{ws}}{a_{ws}}\frac{e^2}{4\pi\epsilon_0 m_i a_{ws}^2}\left(1+\frac{a_{ws}}{\lambda_D}\right)\exp(-a_{ws}/\lambda_D). \\ &= a_{ws}\omega_p^2\left(1+\frac{a_{ws}}{\lambda_D}\right)\exp(-a_{ws}/\lambda_D). \\ &= a_{ws}\omega_p^2\,(1+\kappa)\exp(-\kappa) \\ &= a_{ws}\omega_p^2 \mathrm{G}_2(\kappa) \end{aligned} \tag{2.9}$$

To review, the nearest neighbor model, Eq. 2.9, and the model derived from the MD simulation, Eq. 2.6 , are very similar. Because G_1 and G_2 are weak function of density ($\kappa \approx n^{1/6}$), most of the important density dependence is in the $a_{ws}\omega_p^2$ term ($\approx n^{2/3}$). Figure 2.1 compares the MD model, Eq. 2.6, to the nearest neighbor model, Eq. 2.9. They are quite similar in shape.

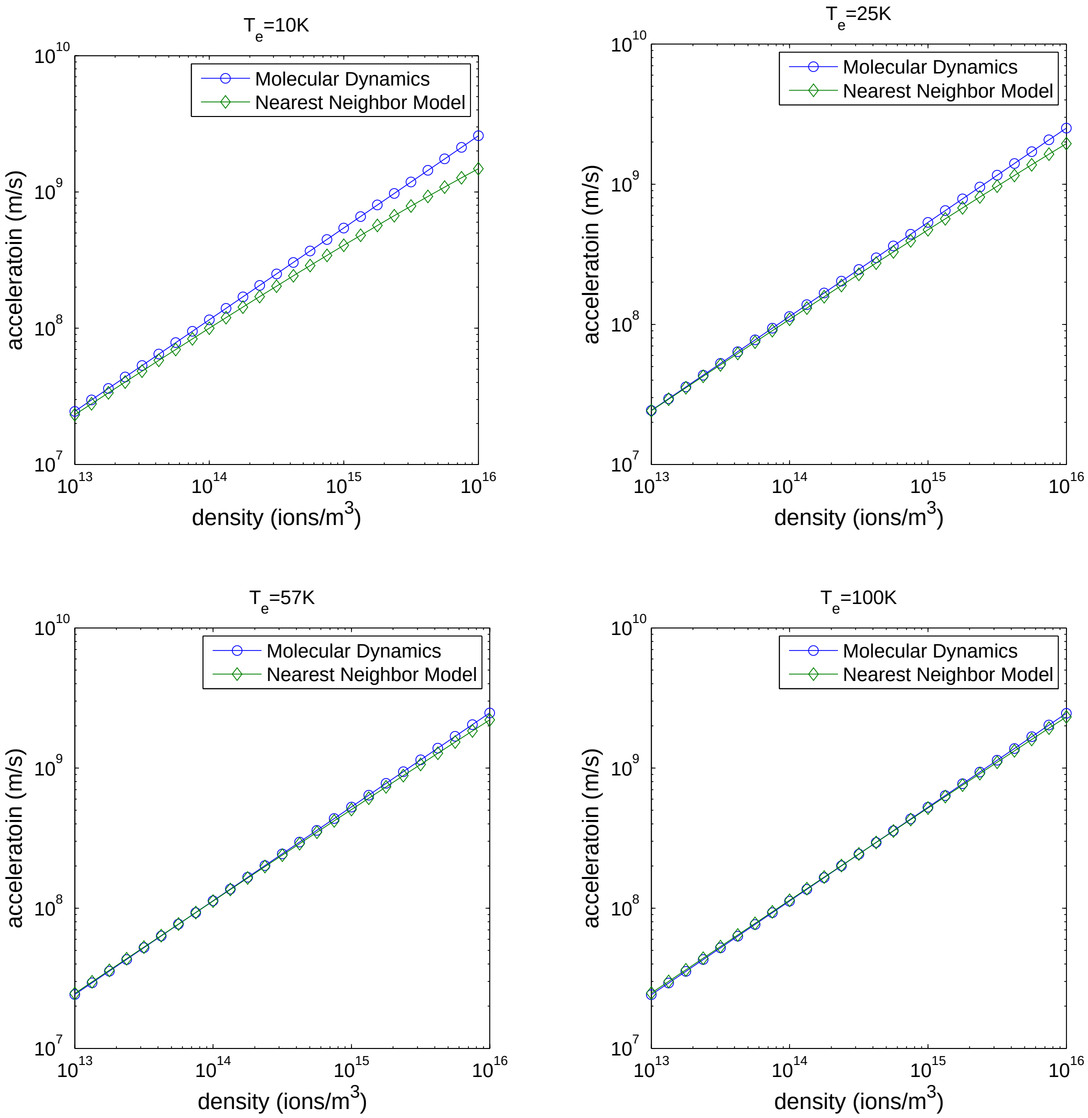

Figure 2.1 A plot of the initial ion acceleration vs. density for four different different electron temperatures. The molecular dynamics simulation and the nearest neighbor model data have been scaled to match at a density of 10^{13} per m^3. Lower electron temperature and higher density correspond to a larger $\kappa \equiv a_{ws}/\lambda_D = n^{1/6}(9/16\pi^2)^{1/3}(e^2/\epsilon_0 k_B T_e)^{1/2}$.

Chapter 3

Experimental Details

The experiment is a labyrinth of hoses, mirrors, electronics, lasers, cooling systems, and vacuums systems. A great deal must be learned before turning the experiment on at all. Much time has been spent making adjustments for optimal performance or completing modifications to improve stability and control. We now describe the major components and processes needed to create a plasma. A photograph of the experiment is shown in Fig. 3.1.

3.1 The Process of Plasma Formation

Calcium was chosen for this experiment because it has a relatively simple two-electron valance shell, and the lasers required for the proper energy level transitions are readily attainable. Figures 3.2 and 3.3 show partial Ca I and Ca II energy level diagrams. Relevant wavelengths and wave-numbers are included.

The experiment takes place in a high vacuum environment. Atmospheric pressure is 10^8 times more dense than our highest density plasmas. The stainless steel vacuum chamber is connected to a turbo pump system. During the initial pump down, when

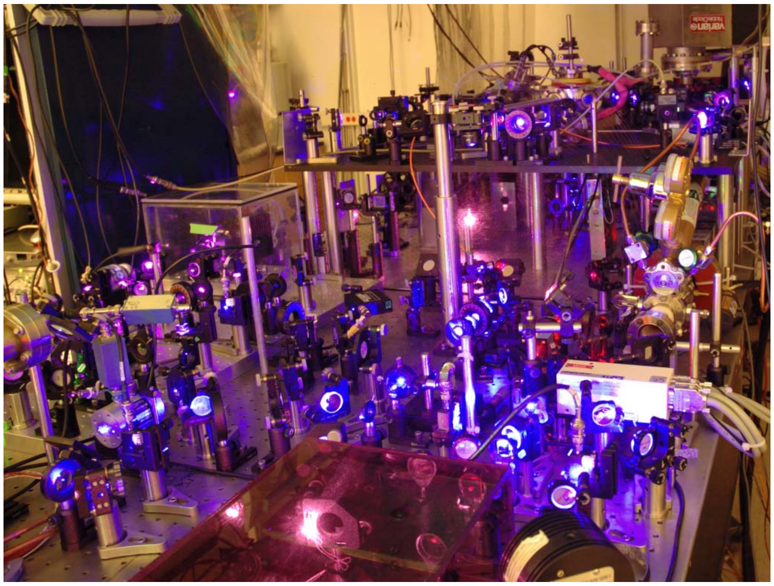

Figure 3.1 A photograph of the experiment. The laser frequency and polarization control optics are shown in the foreground. The MOT chamber is shown in the background.

a pressure of 10^{-5} Torr is reached the turbo pump may be turned off and an ion pump is used to create and maintain a vacuum of 10^{-8} Torr. To add atoms to the chamber, a temperature controlled oven heats a small block of calcium to 860 K. Atoms leave the oven through a 1 mm diameter, 10 mm long nozzle, generating an atomic beam of neutral calcium atoms. These atoms are cooled to 1 mK and confined to a spherical volume with diameter less than 1 mm. Cooling and confining is done simultaneously with a magneto-optical trap (MOT).

A magneto-optical trap consists of a spherical quadruple magnetic field and polarized lasers. Two magnetic field coils are set in the anti-Helmholtz configuration (axially aligned with opposing currents). The resulting magnetic field has a zero in the geometric center but its magnitude increases linearly in the radial direction (a spherical quadruple field). Three-dimensional trapping requires six circularly polarized laser beams. We use three pairs of mutually orthogonal, counter propagating

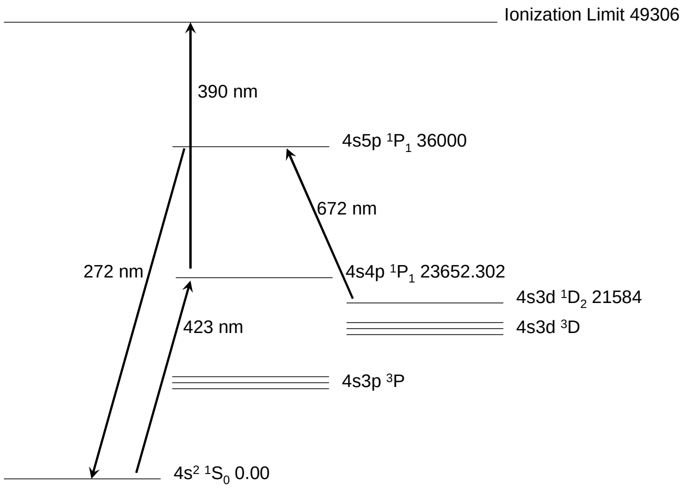

Figure 3.2 A partial energy level diagram of Ca I showing the MOT laser (423 nm), repumper (672 nm), ionization laser (390 nm), and fluorescence wavelengths.

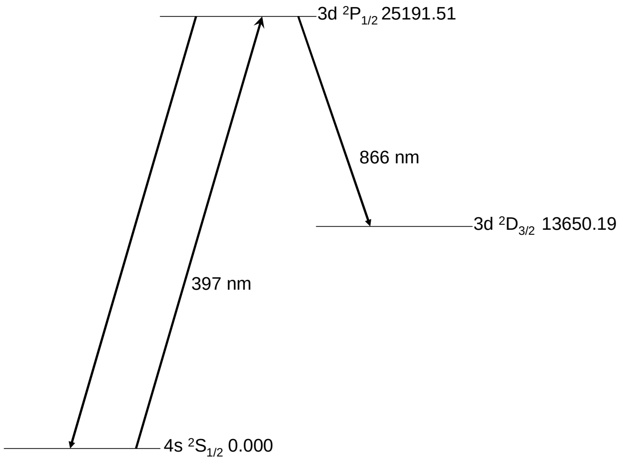

Figure 3.3 A partial energy level diagram of Ca II showing the probe laser wavelength (397 nm) and fluorescence decay (397 nm and 866 nm).

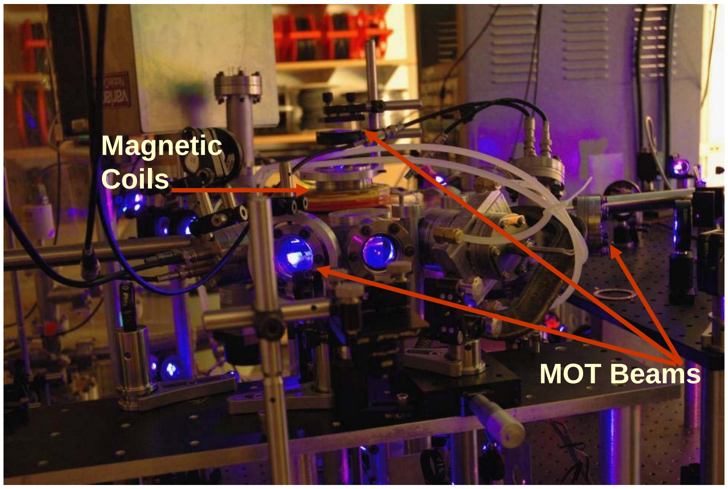

Figure 3.4 Photograph of the vacuum chamber, magnetic coils, and position of MOT beams.

laser beams in which the polarity of the electric fields rotate in opposite directions. All laser beams are detuned one atomic line-width below resonance. A photograph of the vacuum chamber, the magnetic coils, and the MOT beams can be seen in Fig. 3.4.

Explanation of the how the MOT works is easiest in one dimension. The atomic energy levels of the neutral atoms are Zeeman shifted with the spatially varying magnetic field. When an atom reaches a distance from the center of the trap where its energy shift is nearly equal to the detuning of the trapping beam, the probability of photon absorption increases if the quantum mechanical selection rules are met.

Absorption of a $\sigma+$ ($\sigma-$) photon puts the atom in the m= 1 (m= -1) excited state, see Fig.3.5. Atoms at the edge of the trap absorb photons and are pushed back towards the center of the trap. The spatial dependence of the Zeeman shift combined with laser beams creates a trap. The size of the trap can be modified by detuning the trapping lasers or adjusting the amplitude of the magnetic field. Figure 3.5 illustrates the spatial dependence of Zeeman energy splitting and the one-

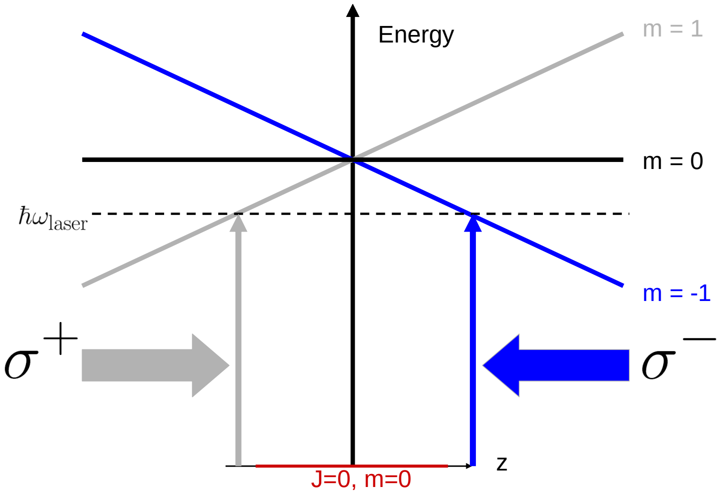

Figure 3.5 A schematic diagram showing the MOT operating principles. The horizontal arrows represent circularly polarized laser beams red-detuned from the atomic transition. The vertical arrows represent the excitation of the neutral atoms. Excitation occurs when the magnetic sublevels of the excited state are Zeeman-shifted into resonance with the laser. Neutral atoms absorb photons according to the quantum mechanical selection rules. Atoms in the negative z direction will only absorb right circularly polarized photons. Atoms on the positive side of z will only absorb left circularly polarized photons.

dimensional confinement process in a MOT. A photograph of the MOT is shown in Fig. 3.6 where the small cloud of atoms emits fluorescence inside the chamber.

Two valuable modifications that increase the density of the atomic cloud are the slowing laser and the repumper laser. The slowing laser is on axis with the atomic beam. This laser is detuned 4 line widths, 140 MHz, below neutral calcium resonance. In the reference frame of some of the atoms traveling in the beam, the slowing laser is Doppler shifted into resonance, increasing the likelihood of photon absorption. Absorption decreases the velocity of the atoms via momentum transfer until the atoms are in a moving slowly enough to become captured by the MOT. Using the slowing laser beam dramatically increases the number of atoms in the MOT.

The repumper laser beam at wavelength 672 nm prevents atoms from falling into a

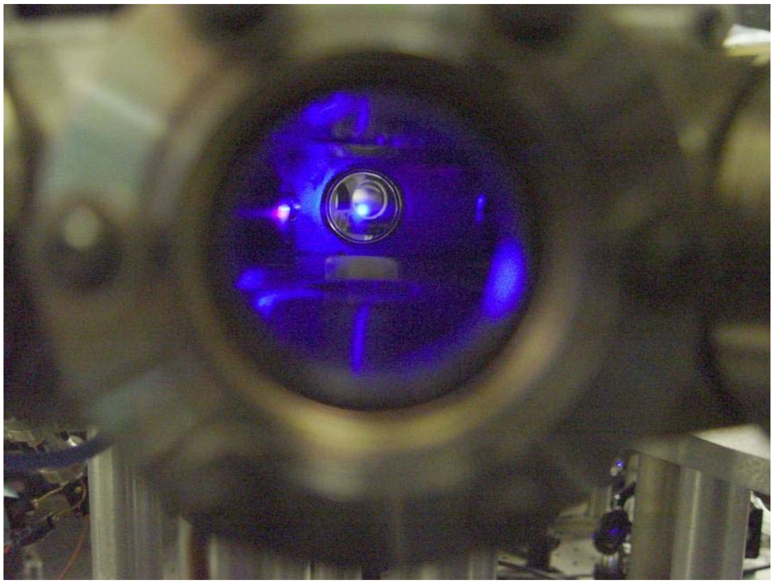

Figure 3.6 A photograph of atoms in the MOT. The small, bright blue spot in the center of the photograph is light scattered by 10^7 calcium atoms cooled to 1 mK confined in a MOT with a 1D rms size of 350 μm.

metastable state (see Fig. 3.2). Most of the trapped atoms are continuously absorbing photons from the MOT laser beams and returning to the ground state. However, each of the excited atoms have a 1 in 10^5 chance to decay via the ${}^1D$ and ${}^3D$ levels to the ${}^3P_0$ and ${}^3P_2$ states where they are lost from the trap. Atoms in these metastable states do not interact with MOT laser beams. This optical leak decreases the density of neutral atoms in the MOT and therefore reduces the maximum ion density. The repuming beam illuminates the entire MOT. As atoms decay into the ${}^1D_2$ state they are quickly pumped back into an excited state which decays to the ground state. There are other states into which the excited neutral atoms may decay. Adding additional repumpers for these states would not provide much of a performance increase because decaying to these states is less probable.

Once the neutral atoms are trapped and cooled they are photo-ionized using counter-propagating laser pulses with wavelengths of 423 nm and 390 nm. The pulses energies are of 10 μJ and 20 mJ, respectively during a 3 ns pulse duration. Typical values of ionization efficiency are around 90%. Adjusting the ionizing laser frequency varies the electron temperature of the plasma. Because calcium ions are $\approx 70,000$ times more massive than electrons, most of the energy above ionization is transferred to the electrons increasing the electron temperature. Density can be varied by changing the power of the ionizing beams. Decreasing the power decreases the number of ions excited but the volume in which the ions reside is constant.

3.2 Measuring Ion Dynamics

We simultaneously determine the evolving plasma density and ion velocity. For this we use both absorption and fluorescence spectroscopy (see Sec. 1.3). Since we are only interested in the early times in the plasma, we only need to record the first micro-second after ionization. The entire measurement cycle is repeated at a rate of 10Hz. Both absorption and fluorescence signals are measured and averaged 300 times by an oscilloscope and then recorded in digital format for data processing.

Absorption spectroscopy is ideal for density determination. A 423 nm probe laser is directed through the center of the MOT before and after ionization. Later the optical depth is calculated from the transmission signal $\mathrm{T} = 1 - \mathrm{A}$, where A is the absorbance, and related to a peak density with Eq. 1.3. Figure 3.7 shows an example of the experimental transmission of the 423 nm probe beam as a function of time.

Mathematically the transmission of the 423 nm probe laser beam is

$$\mathrm{T} = \exp\left[-\int n\alpha(\nu)dz\right], \tag{3.1}$$

and the optical depth is

$$\ln(\mathrm{T}) = -\int n\alpha(\nu)dz. \tag{3.2}$$

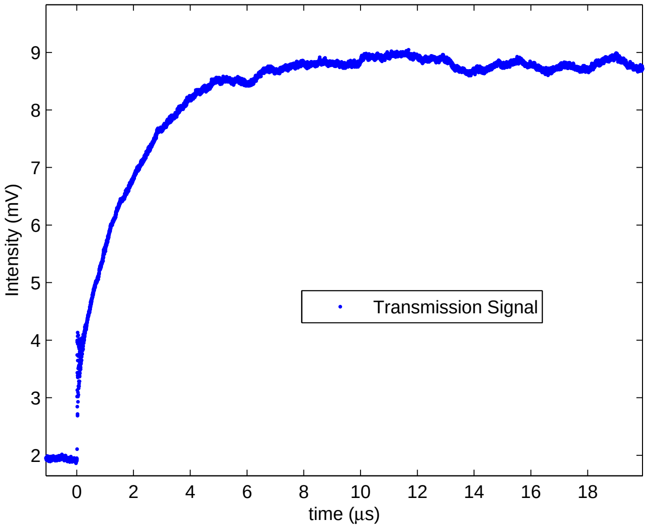

Figure 3.7 Transmission of the 423 nm probe laser beam through the plasma as a function of time. Time $t = 0$ is the time of ionization

During the initial plasma period the time dependence of the Gaussian density profile, Eq. 1.1, can be neglected. If the laser is directed through the geometric center ($x = y = 0$), the density profile in the z direction may be written as $n = n_0 \exp{(-z^2/2\sigma^2)}$. The difference in optical depth before and after ionization is

$$\begin{aligned} \ln(\mathrm{T}_a) - \ln(\mathrm{T}_b) &= -\int n_{0a} \exp{(-z^2/2\sigma^2)} \alpha(\nu) dz + \int n_{0b} \exp{(-z^2/2\sigma^2)} \alpha(\nu) dz \\ &= (n_{0b} - n_{0a}) \left[\int \exp{(-z^2/2\sigma^2)} \alpha(\nu) dz \right], \end{aligned} \tag{3.3}$$

where the subscripts b and a are labels for before and after respectively. The peak plasma density is equal to the change in MOT density

$$n_{0i} = n_{0b} - n_{0a} = \frac{\ln(\mathrm{T}_b/\mathrm{T}_a)}{\int \exp{(-z^2/2\sigma^2)} \alpha(\nu) dz}, \tag{3.4}$$

illustrating that the plasma density is proportional to the log of ratio of transmitted 423 intensity before and after ionization of the MOT. The denominator in Eq. 3.4

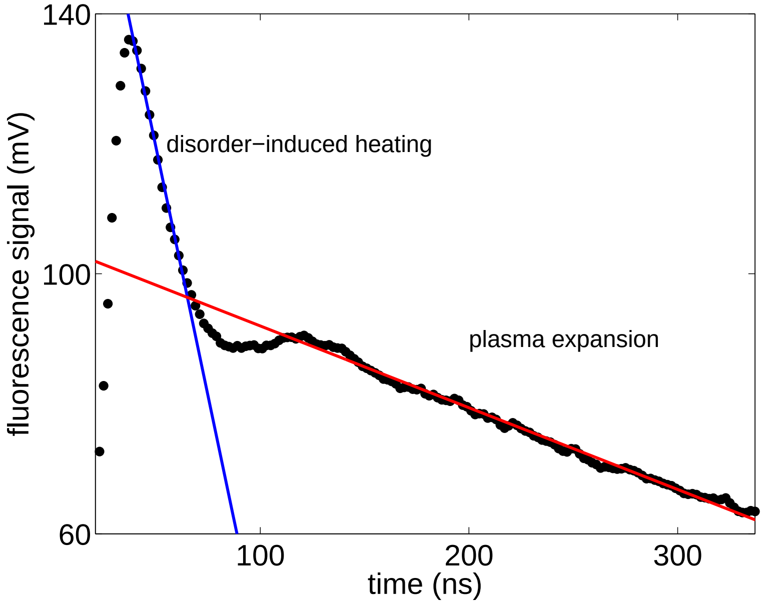

Figure 3.8 Measured ion fluorescence from the plasma (black circles). Disorder-induced heating and plasma expansion occur over different time scales, as shown by the blue and red lines, respectively.

can be simplified

$$\int \exp\left(-z^2/2\sigma^2\right)\alpha(\nu)dz = \frac{3\lambda^2\sigma}{\sqrt{2\pi}}, \tag{3.5}$$

where it is assumed the probe laser beam is exactly on resonance with the ions and the absorption cross section is $\alpha(0) = 3\lambda^2/2\pi$. Equation 3.4 becomes

$$n_{0i} = \frac{\sqrt{2\pi}\ln(\mathrm{T}_b/\mathrm{T}_a)}{3\sigma\lambda^2}. \tag{3.6}$$

Fluorescence is used to determine the velocity of the ions. A 397 nm probe laser beam tuned to the first resonance transition of the ions is sent through the center of the plasma. Typical fluorescence data are shown in Fig. 3.8.

Using classical absorption theory, the fluorescence signal can be converted into a velocity. The Voigt profile is a convolution of the Lorentzian and Gaussian lineshapes,

$$\begin{aligned} V(f') &= \int_{-\infty}^{+\infty} L(f-f')G(f)df \\ &= \int_{-\infty}^{+\infty} \frac{\Delta\nu_L/2\pi}{(f-f')^2+\Delta\nu_L^2/4}\cdot\frac{1}{\sqrt{2\pi}\Delta\nu_D}\exp(-f^2/2\Delta\nu_D^2)df \qquad (3.7) \end{aligned}$$

where f' is the frequency detuning from resonance, $\Delta\nu_L$ is the FWHM Lorentzian linewidth, and $\Delta\nu_D$ is the rms Doppler width. When $f'=0$, exactly on resonance, Eq. 3.7 can be integrated

$$V(0) = \frac{1}{\sqrt{2\pi}\Delta\nu_D}\exp\left(\frac{\Delta\nu_L^2}{8\Delta\nu_D^2}\right)\mathrm{erfc}\left(\frac{\Delta\nu_L}{\sqrt{8}\Delta\nu_D}\right). \qquad (3.8)$$

After substituting $\Delta\nu_L = v_n/\lambda$ and $\Delta\nu_D = v_{th}/\lambda$ Eq, 3.8 becomes

$$V(0) = \frac{k}{v_{th}}\exp\left(\frac{v_n^2}{8v_{th}^2}\right)\mathrm{erfc}\left(\frac{v_n}{\sqrt{8}v_{th}}\right), \qquad (3.9)$$

where k is a proportionality constant, $v_n = \Delta\nu_L\lambda = \lambda/2\pi\tau = 8.9$ m/s is the natural velocity (the velocity for which the doppler shift equals the Lorenztian FWHM), $v_{th} = \sqrt{k_B T_i/m_i} = \Delta\nu_D\lambda$ is the rms thermal velocity, and erfc is the complimentary error function. The initial neutral atom velocity is near the Doppler limit 0.5 m/s [6]. In principle the velocity of the atoms is further increased upon ionization by the photon recoil velocity $v_r = h/m_i\lambda$, however the ionizing laser beams are counter propagating and near the same wavelength. Therefore the sum of the ionizing recoil velocities is negligible and the initial ion velocity is 0.5 m/s (the velocity of the neutral atoms). With known initial velocity, Eq. 3.9 can be solved numerically. The proportionality constant is chosen so that the data is linearly extrapolated to be 0.5 m/s at time $t = 0$ (time of ionization). Figure 3.9 shows the rms thermal velocity of the ions during the first 300 ns. The DIH and expansion phases are clearly visible.

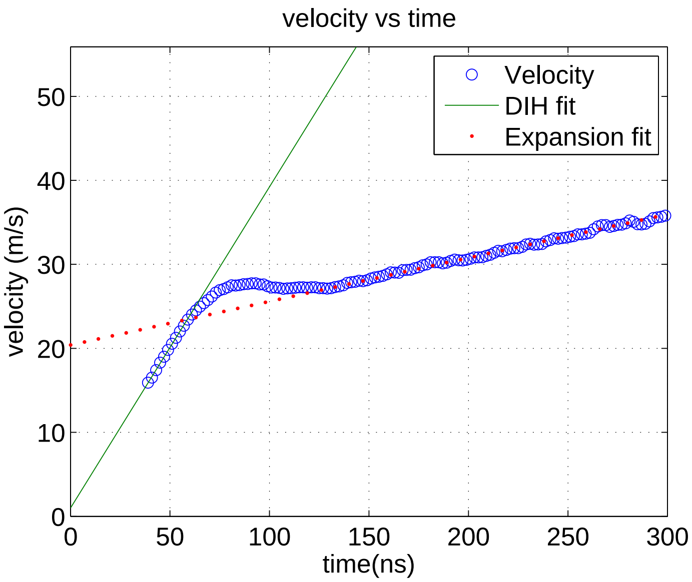

Figure 3.9 The rms thermal velocity during the first 300 ns. The solid fitted line represents the DIH phase. The slope of the velocity is the acceleration of the average ions.

The MD model (Eq. 2.6) suggests the initial ion acceleration should be constant in time (the MD model is only valid for early time scales), therefore the acceleration during the DIH phase can be calculated as the slope of the velocity in time.

Our ananlysis method is insensitive to the variation in probe intensity because we the measure the slope of signal, not the absolute signal.

The analysis is sensitive to the laser position and detuning of the ion probe laser beam. To minimize detuning problems the probe laser beam detuning is optimized repeatedly through out the measurement session. The variation in laser position is negligible because through out the day alignment changes are small compared to the initial plasma size.

3.3 The Author's Contribution to This Work

As with many projects, this thesis builds on a foundation laid by others. The experimental apparatus was operational before this thesis project began. The author spent several months mastering the day-to-day operational details of the experiment. He helped initiate this particular project. He optimized the MOT operation, laser performance, and data acquisition, and wrote the computer programs to analyze the data as outlined in Sec. 3.2.

Chapter 4

Data and Discussion

We measured the fluorescence signal during DIH plasmas for a various electron temperatures and initial plasma densities. We assumed the initial plasma density to be constant over the DIH phase. As discussed in section 3.2, we use our lineshape model, Eq. 3.9, to determine the rms ion velocity as a function of time. The slope of the velocity in time during DIH is the initial ion acceleration. Figure 4.1 shows the experimental and theoretical relationship of DIH acceleration versus density for two electron temperatures.

The open and closed data points represent electron temperatures of 1 K and 57 K respectively. The fitted curves are the scaled theoretical model derived from results of the molecular dynamics simulation, Eq. 2.6. The experimental data agrees well at low densities, though for larger densities it is apparent the data does not fit the model.

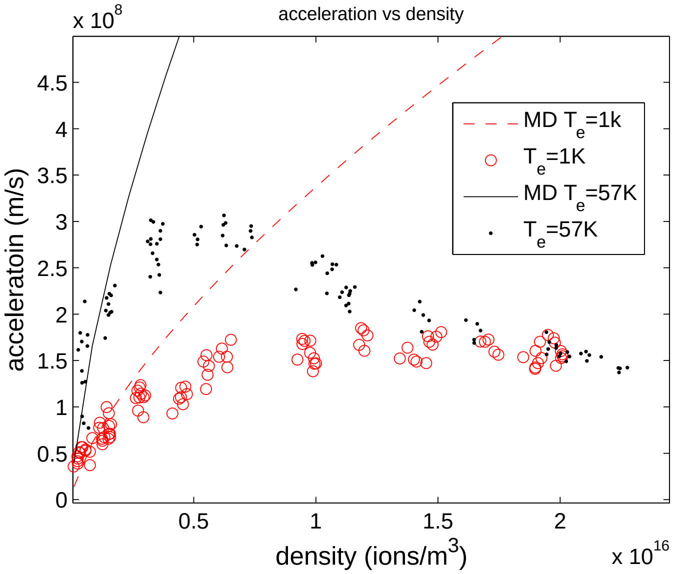

Figure 4.1 The acceleration vs density for two initial electron temperatures. MD is a scaled theoretical model resulting from a molecular dynamics simulation.

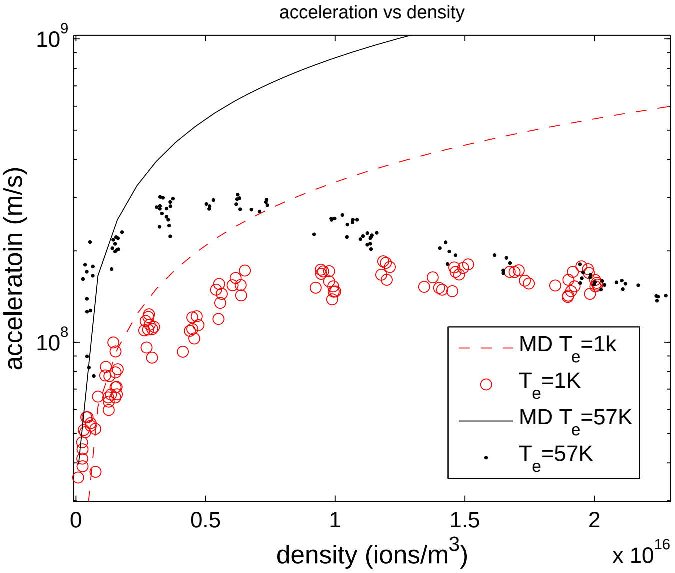

Figure 4.2 A semi-log plot acceleration vs. density including the scaled molecular dynamics model.

4.1 Experimental Substantiation

There are two categories of experimental errors which may explain the discrepancies in Sec. 4. These are problems with the 397 nm fluorescence probe beam such as power broadening, detuning, and optical depth issues, or problems that may affect the actual ion density such as ionizing beam detuning or atoms being excited into a state in which there is little interaction with the fluorescence probe.

If the ion probe laser beam is intense enough the ion linewidth will be power broadened. Power broadening has a Lorenztian line shape,

$$S(\nu, I) = \frac{s/2}{(\nu - \nu_0)^2 + 1 + s},, \tag{4.1}$$

where $s = I/Isat$, and $\Delta\nu_P = 2\sqrt{1+s}$ (FWHM). The fluorescence spectroscopy technique assumes that Doppler broadening is the only broadening mechanism of the atomic transitions. Any contributions by power broadening will decrease the accuracy of acceleration measurement. The experimental saturation intensity of the 397 nm ion transition is 48 mW/cm^2. For our beam waist of 100 μm, the saturation intensity is 7.5 μW. Laser power this low is below equipment threshold to directly and accurately make a measurement, however, we have reduced the probe laser intensity until the fluorescence signal is independent of the probe laser beam power. This suggests the power of the probe beam is below saturation intensity. In addition, plasma oscillations, that are clearly seen in the fluorescence signal, would not be resolved if the fluorescence line was power broadened.

The fluorescence analysis (Eq. 3.9) assumes that the probe laser beam is exactly on resonance with the ions atomic transition. We use the DAVLL technique [8] to the lock the laser to the ion [6]. The precise line center is found by maximizing the fluorescence signal. If the laser is detuned from resonance the fluorescence signal will appear to correspond to a smaller acceleration.

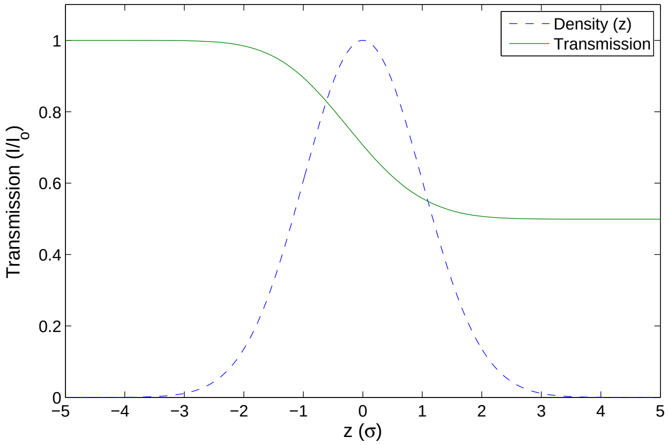

Figure 4.3 The probe laser beam transmission through a one-dimensional Gaussian plasma on resonance.

Optical depth may be an issue. In high density plasmas the laser beam would be attenuated before reaching the center of the plasma where it may interact at peak density. If this is the case we would only be probing the acceleration at the low densities of the outer region of the plasma where the ions accelerate more slowly.

We have performed optical depth measurements using the ion probe beam in which the maximum transmission was around 50%. Figure 4.3 shows the theoretical on resonance laser beam intensity through a one-dimensional Gaussian plasma. The dashed line is a Gaussian density profile of which 50% of the initial intensity is transmitted.

The effective density averaged along the attenuated probe laser beam is smaller by a factor of

$$n_p = \frac{\int (I/I_0) n(z) dz}{\int n(z) dz}, \tag{4.2}$$

where $n(z)$ is a gaussian density profile, I/I_0 is the transmission, and I_0 is the peak initial intensity. When the transmission is 50 %, the effective density is $0.72 n_0$ and $a_{ws}\omega_p^2$ is reduced by a factor of $0.72^{2/3} = 0.80$. This cannot explain the factor of 10 discrepancy between the model and the experiment in Fig. 4.2.

There may be an apparent ion density decrease due to optical pumping into the $^3D_{3/2}$ state (see Fig.3.3). We have established that the ion probe laser beam is below saturation intensity, however, for the worst case scenario it will be considered here. The $^2P_{1/2}$ excited state of the ion has a lifetime of $\tau = 7$ns. If the ion line is in saturation it will take time $= 2\tau = 14$ ns to absorb and emit a photon. The branching fraction that decays to the metastable $^3\mathrm{D}_{3/2}$ state is $\mathrm{BF}_m = 1/17$. The time taken for the ion density to decrease by a factor of $1/e$ is $t = \tau/\mathrm{BF}= (17) * (14)$ ns = 238 ns. Optical pumping decreases the density a negligible amount and it takes a time period approximately twice as long as the plasma period. This is long after the slope of the velocity in time has been determined.

4.2 Physical Processes

One possible explanation for the discrepancy is that during a short time after ionization the plasma undergoes rapid three body recombination. The three body recombination rate as a function of electron temperature and density is

$$R_e = n^2 T_e^{-9/2} \left(\frac{e^2}{4\pi\epsilon_0 k_B} \right)^5 \sqrt{\frac{k_B}{m_e}} \tag{4.3}$$

where m_e is the mass of the electron and all other variables and constants have been previously been introduced. In the process of three body recombination an ion recaptures an electron. These electrons typically lie in high energy states that are effective at shielding other ions. This makes the potential landscape more shallow which will make the ions accelerate more slowly. Recombination could also explain why higher electron temperature plasmas follow the theoretical curve better. The recombination rate decreases for higher temperatures but increases with density. At low densities the electron temperature can offset the functional dependence on density where the model is followed most closely. Plasmas with high electron temperatures reduce the Recombination rate more and are able to follow the model better for higher densities.

Although recombination appears to be a promising explanation it may be quickly discarded with a simple calculation. Using Eq. 4.3, the three body recombination rate of plasma with density of 10^{16} ions per m^3, and electron temperature of 57 K, is on the order of 5000 s^{-1}, making the characteristic time 200 μs. For three body recombination to explain the discrepancy a significant amount would have to occur before the first 50 ns, the time at which the slope of the velocity is well defined.

Electron screening could be responsible for the discrepancy. Nearest neighbor interaction is the dominating factor during DIH acceleration. If the screening length is less than the average distance between ions, a_{ws}, the potential landscape will be diminished and DIH will proceed more slowly . Figure 4.4 is a theoretical plot of $\kappa = a_{ws}/\lambda_D$ over a density range similar to the experiment. Three electron temperatures are featured. Values of κ greater than one have screening lengths smaller than a_{ws}. The notion of electron screening causing the discrepancy can be discarded upon examination of the 57 K data. Figure 4.4 shows the screening length increases with density but is always larger than the distance between particles. However, the 57 K data shown in Fig. 4.1 shows the experimental acceleration to be less than the model over a similar range of densities.

An accelerating charged particle radiates. A logical explanation may be that the missing kinetic energy may be ascertained to radiative losses. Lets consider a two particle model in which a test particle is accelerated in a Yukawa potential

$$U(r) = \frac{\exp(-r/\lambda_D)}{4\pi\epsilon_0 r}. \tag{4.4}$$

The energy lost as radiation by an accelerating charged particle is the power radiated

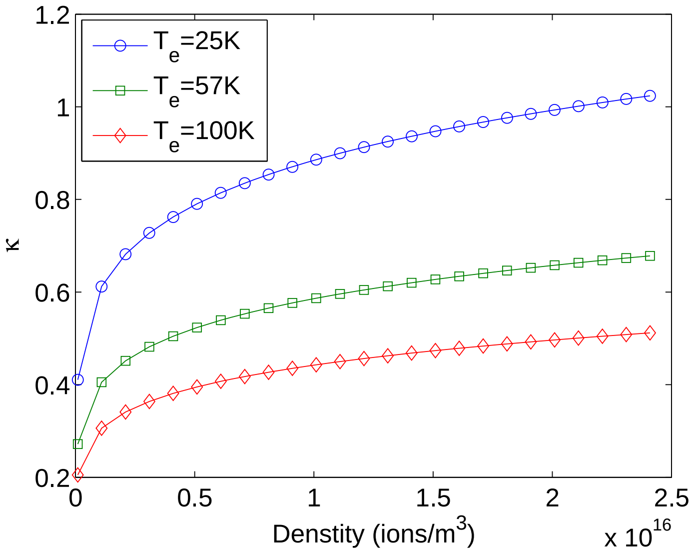

Figure 4.4 A plot of κ over the experimental density range. Values of κ greater than 1 correspond to screening lengths smaller than the average distance between particles.

multiplied by the period of radiation

$$E_{rad}(t) = \frac{e^2 a^2 t}{6\pi\epsilon_0 c^3}, \tag{4.5}$$

where it is assumed the acceleration is constant in time. If the ratio of the potential to radiative energy is on the order of 1 or less the radiative energy loss will make a significant deduction from the energy landscape. The ratio is

$$\frac{U(r)}{E_{rad}(t)} = \frac{3c^3 \exp\left(-r/\lambda_D\right)}{2re^2a^2t}. \tag{4.6}$$

Evaluating Eq. 4.6 for a typical plasma with density $n = 10^{16}$, $r = a_{ws}$= 2.9 μm, acceleration $a = 10^8$ m/s^2, initial electron temperature T_e=57 K, and radiation time $t = 50$ ns yields a ratio of the order 10^{60}. The energy lost to radiation is negligible.

In conclusion we have measured ion accelerations during the DIH phase that do not scale with density as predicted by the best current theories. The cause of this effect is clearly outside the models and simulations. We have shown that this effect is not caused by ion radiation, by optical pumping, or by power broadening. It cannot be explained by shielding or nearest-neighbor interactions. It also is not caused by the increased optical depth of the plasma. While it's cause is as yet unknown, it may be related to nonlinear screening by the electrons or to electron-ion correlations.

Bibliography

[1] S. Kulin, T.C. Killian, S.D. Bergeson, and S.L. Rolston, Phys. Rev. Lett. **85**, 318 (2000)

[2] T.C. Killian, S. Kulin, S.D. Bergeson, L.A. Orozco, and S.L. Rolston, Phys. Rev. Lett. **83**, 4776 (1999)

[3] P. Gupta, S. Laha, C. E. Simien, H. Gao, J. Castro, and T. C. Killian, Phys. Rev. Lett. **99**, 075005 (2007).

[4] S. D. Bergeson and R. L. Spencer, Phys. Rev. E **67**, 026414 (2003).

[5] C.E. Simien, Y.C. Chen, P. Gupta, S. Laha, Y.N. Martinez, P.G. Mickelson, S.B. Nagel, and T.C. Killian Phys. Rev. Lett. **92**, 143001 (2004).

[6] E.A. Cummings, J.E. Daily, D.S. Durfee, and S.D. Bergeson, Phys. Rev. Lett. **95**, 235001 (2005)

[7] M. S. Murillo, Phys. Rev. Lett. **96**, 165001 (2006).

[8] K. L. Corwin, Z. T. Lu, C. F. Hand, R. J. Epstein and C. E. Wieman Appl. Opt. **37**, 3295 (1998).